FULL PAPER

All-Solution-Processed Indium-Free Transparent Composite Electrodes based on Ag Nanowire and Metal Oxide for Thin-Film Solar Cells

Areum Kim, Yulim Won, Kyoohee Woo, Sunho Jeong, and Jooho Moon*

Fully solution-processed Al-doped ZnO/silver nanowire (AgNW)/Al-doped ZnO/ZnO multi-stacked composite electrodes are introduced as a transparent, conductive window layer for thin-film solar cells. Unlike conventional sol–gel synthetic pathways, a newly developed combustion reaction-based sol–gel chemical approach allows dense and uniform composite electrodes at temperatures as low as 200 °C. The resulting composite layer exhibits high transmittance (93.4% at 550 nm) and low sheet resistance (11.3 Ω sq^{-1}), which are far superior to those of other solution-processed transparent electrodes and are comparable to their sputtered counterparts. Conductive atomic force microscopy reveals that the multi-stacked metal-oxide layers embedded with the AgNWs enhance the photocarrier collection efficiency by broadening the lateral conduction range. This as-developed composite electrode is successfully applied in $Cu(In_{1-x}Ga_x)S_2$ (CIGS) thin-film solar cells and exhibits a power conversion efficiency of 11.03%. The fully solution-processed indium-free composite films demonstrate not only good performance as transparent electrodes but also the potential for applications in various optoelectronic and photovoltaic devices as a cost-effective and sustainable alternative electrode.

1. Introduction

Transparent electrodes are among the most important components in developing various optoelectronic devices including thin-film solar cells, touch screens, and light-emitting diodes for displays and smart windows.[1] Thin-film solar cells require transparent electrodes that can provide large-area processability and cost-effectiveness with high transparency and conductivity. Currently, indium tin oxide (ITO) is the most commonly used transparent electrode material and over the last four decades has demonstrated excellent conductivity (≈10^3 S cm^{-1}) and transparency (≈90% at 550 nm).[2,3] However,

ITO is undesirable for large-area, low-cost solar cells due to the scarcity of indium and its expensive vacuum deposition-based fabrication method. Alternatively, a variety of materials have been investigated, including silver nanowire (AgNW) films,[4] metallic grids,[5] conjugated polymers,[6] carbon nanotubes (CNTs),[7–9] and graphenes.[10,11]

Among these materials, AgNW films are an attractive candidate due to their outstanding optical and electrical properties. AgNW films can also be easily deposited on various target substrates via scalable coating or printing methods. A solution-processed deposition method can provide a variety of appealing advantages such as simplicity, low cost, and high throughput. Lee et al. was the first to demonstrate a solution-processed, randomly dispersed AgNW mesh with low sheet resistance and high transmittance as a promising transparent electrode.[12] However, some issues must be resolved before these AgNW networks can be successfully applied to optoelectronic devices including their i) rough surface finish, ii) poor adhesion to substrates, iii) thermal instability, iv) high junction resistance, and v) limited contact area with the adjacent layer. Recently, hybrid structures composed of an AgNW mesh and a vacuum-deposited conductive metal-oxide layer have been suggested as promising alternatives to resolve these issues.[13] Conductive metal-oxide layers were introduced as an overcoat to protect the AgNWs from local melting-induced disconnection, thus enhancing the thermal stability of the AgNWs. Metal-oxide overcoating layers also improve the adhesiveness of the AgNWs to the substrate. Furthermore, this composite electrode facilitates effective charge-carrier collection by filling the empty space unoccupied by the AgNWs and by smoothing the electrode surfaces.[14]

Chung et al. reported solution-processed transparent hybrid conductors that incorporate AgNW networks embedded in an ITO nanoparticulate layer with a sheet resistance of 23 Ω sq^{-1} and a transmittance of 88.6% at 550 nm.[15] This AgNW–ITO nanoparticle composite electrode could be implemented in $CuInSe_2$ thin-film solar cells to achieve performance comparable to that of sputtered ITO-based devices.[16] However, to date, solution-processed, indium-free composite electrodes for use in thin-film solar cells have not been demonstrated because

A. Kim, Y. Won, Dr. K. Woo, Prof. J. Moon
Department of Materials Science and Engineering
Yonsei University 50 Yonsei-ro
Seodaemun-gu, Seoul 120–749, Republic of Korea
E-mail: jmoon@yonsei.ac.kr
Dr. S. Jeong
Advanced Materials Division
Korea Research Institute of Chemical Technology 19 Sinseongno
Yuseong-gu, Daejeon 305–600, Republic of Korea

Materials
Views

www.MaterialsViews.com

ADVANCED
FUNCTIONAL
MATERIALS
www.afm-journal.de

FULL PAPER

indium is required to generate a sufficient quantity of charge carriers for acceptable electrical conductance. Unlike vacuum-deposited pure dense oxide layers, many structural defects can exist in solution-processed nanoparticulate layers such as impurity moieties surrounding the nanoparticles and grain boundaries between neighboring nanoparticles, which can critically restrict the mobility of the charge carriers; thus, indium is incorporated to improve the electrical conductance by increasing the concentration of charge carriers and overcoming the structural impediments inherent in the particulate films. There have been a few reports on solution-processed AgNW composite electrodes with either ZnO or Al-doped ZnO (AZO) nanoparticles; but they suffered from a relatively low transparency (transmittance of 76–81% at 550 nm) and the electrical properties of composite film were not evaluated.[14,17] As an alternative to nanoparticulate films, sol–gel-derived metal-oxide films can be used as an overcoat layer because a dense film structure can easily be obtained and the impurities can be thermally decomposed through a simple annealing process above 400 °C. However, to fabricate a window layer for $Cu(In_{1-x},Ga_x)$ S_2 (CIGS) solar cells, the precursor solution and the process temperature should be controlled to prevent chemical and/or thermal damage to the underlying absorber and buffer layer. Furthermore, the AgNWs become thermally unstable at elevated temperatures (>225 °C), as the nanowires tend to coalesce into isolated droplet-shaped Ag particles, causing the metallic network structures to collapse.[12,13]

We present, for the first time, indium-free all-solution-processed composite electrodes in which AgNWs are sandwiched between low-temperature processable, sol–gel-derived metal-oxide layers for thin-film solar cells. To produce low-temperature-annealed, transparent conductive metal-oxide layers, we apply a redox-based combustion synthetic approach in which self-generated energy converts the precursors into transparent conductive oxides at 200 °C.[18] Our composite electrodes have an asymmetric structure of Al-doped ZnO(AZO)/AgNW/Al-doped ZnO/ZnO and exhibit a high transmittance of 93.4% at 550 nm with a low sheet resistance of 11.3 Ω sq^{-1}. These material characteristics and structural configurations allow for a successful integration into $Cu(In_{1-x},Ga_x)S_2$ (CIGS) thin-film solar cells, with a cell performance comparable to that of a sputtered ITO/intrinsic (i)-ZnO reference cell. To track the current conduction paths in a composite electrode layer during solar cell operation, the physical attributes of this all-solution-processed composite electrode are examined using conductive atomic force microscopy (C-AFM) under a 0.2 sun illumination.

2. Results and Discussion

We fabricated an AZO/AgNW/AZO/ZnO composite, which is denoted as an A/AgNW/AZ (A: AZO; AgNW: silver nanowire; AZ: AZO/ZnO bilayer) composite, by sequentially stacking transparent conducting oxide (TCO) layers and AgNW films using a simple liquid-phase coating process. The AZO layer was added for improved electrical conductivity to efficiently collect the charge carriers, and the bottom ZnO layer was incorporated as an undoped, intrinsic layer to reduce the current leakage on the top of the buffer layer. In sol–gel-based metal-oxide films,

a high-temperature annealing process is required for the complete hydrolysis and condensation reactions. Most conventional sol-gel-derived AZO films are annealed above 600 °C in air, followed by a post-annealing step at 550 °C in a hydrogen atmosphere, with resistivities ranging from 1.7×10^{-3} to 7.2×10^{-3} Ω cm.[19–21] However, for application in CIGS thin-film solar cells, the annealing temperature should be reduced because the transparent window layer is stacked on the top of cell, and the underlying absorber and n-type buffer layer should undergo the undesirable thermal budget during the process of annealing the window layers. High-temperature annealing can cause performance degradation due to the excessive diffusion of Cd or Zn into the CIGS absorber layer.[22] To confirm that the temperature conditions are acceptable for the solar cell performance, we analyzed thin-film solar cells composed of ITO/i-ZnO/CdS/CIGS/Mo/glass baked in air above 250 °C. The cell performance gradually decreased above 250 °C, as shown in Figure S1 (Supporting Information). Compared with a pristine device, the photoconversion efficiency of the device baked at 250 °C decreased by 13%, while the device baked at 300 °C exhibited a 38% reduction in efficiency. In the pristine device, the transparent electrode was deposited at a substrate temperature of 200 °C, which suggests that an annealing temperature above 200 °C can cause severe degradation of the cell performance.

Combustion sol–gel precursor solutions of ZnO and AZO were synthesized according to the method suggested by Kim et al.[13] with a slight modification to reduce the annealing temperature (see Experimental section for details). In conventional sol–gel reactions, the endothermic process evolves during the conversion of hydroxide/alkoxide into the corresponding metal oxides, while combustion-derived reactions involve highly exothermic self-catalytic precursors. The high internal energy of these combustion precursors can drastically reduce the external energy input required for chemical conversion processes.[23] We used nitrate and acetylacetonate precursors as an oxidizer and fuel, respectively. As shown in **Figure 1**, for combustion sol–gel-derived AZO and ZnO precursor solutions, sharp exothermal peaks were observed at 190 °C with an abrupt weight loss due to the instant condensation reaction for the oxide phase formation. For the conventional sol–gel-derived ZnO and AZO precursor solutions, no exothermal peaks or abrupt weight loss were detected. The X-ray diffraction (XRD) data suggest the formation of crystallized oxide phases with a combustion-based sol-gel reaction by annealing at temperatures as low as 200 °C, while amorphous phases persisted for the conventional sol–gel-derived ZnO and AZO films as shown in **Figure 2**. The sheet resistance (R_S) of the conventional sol–gel-based ZnO and AZO films exceeded 10^9 Ω sq^{-1}, the measurement limit of our 4-point probe, whereas the R_S values of the combustion-assisted ZnO and AZO films were measured at approximately 15×10^6 Ω sq^{-1} and 3.26×10^8 Ω sq^{-1} with electrical resistivities of 210 Ω cm and 4450 Ω cm, respectively. Even with the combustion-based chemical methodology, the resistivity remains high due to the incomplete electronic structural evolution at the low temperature of 200 °C. Although the metal-oxide framework skeleton is effectively achieved by a sufficient supply of thermal energy from a combustion reaction, the temperature-dependent evolution of the charge carriers is not sufficient to improve the electrical conductivity at 200 °C.
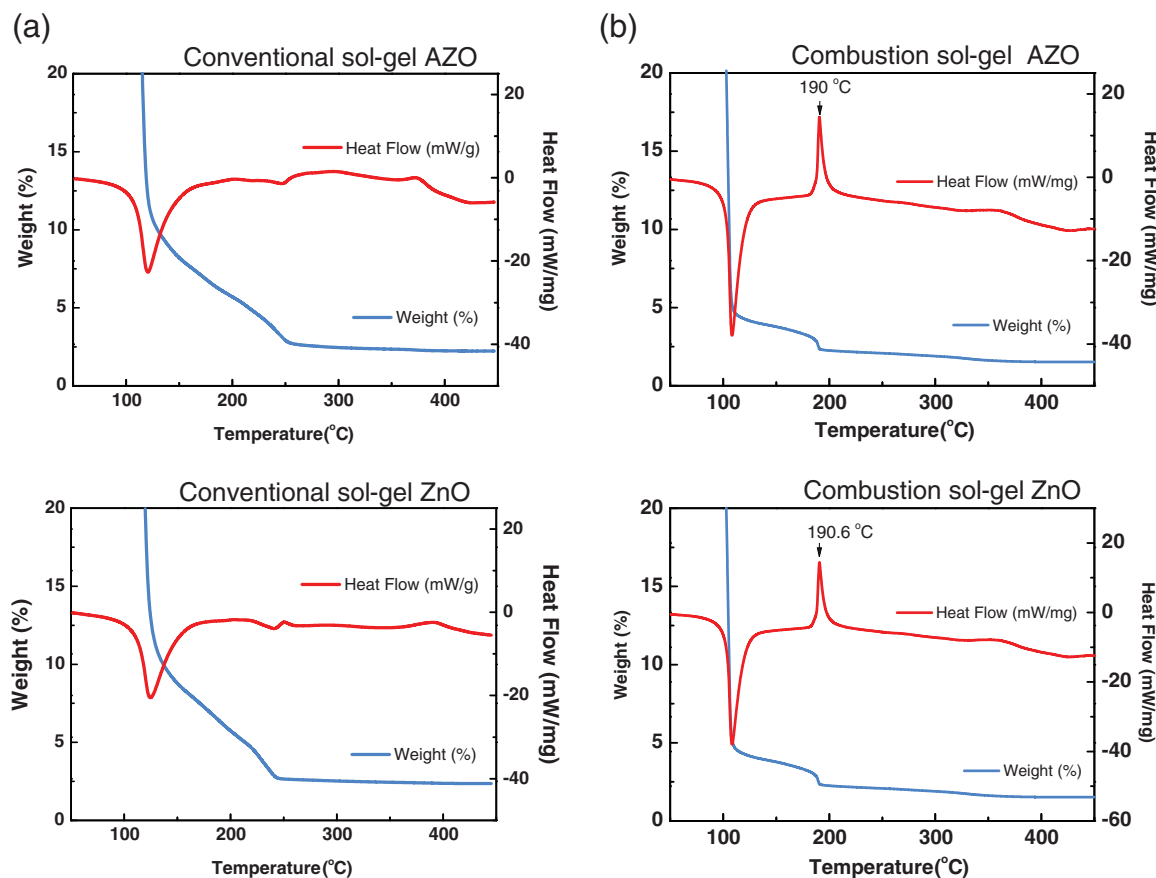
**ADVANCED
FUNCTIONAL
MATERIALS**

www.afm-journal.de

*Materials
Views*

www.MaterialsViews.com

FULL PAPER

Figure 1. Thermogravimetry-differential scanning calorimetry (TG-DSC) analysis of a) conventional sol–gel-based aluminum-doped ZnO and ZnO and b) their combustion-assisted sol–gel precursor-derived counterparts.

Figure 3a presents the surface structure of the A/AgNW/AZ composite electrode. The AZO layer was selected as a matrix for AgNWs networks, instead of ZnO, since it showed better conductivity as mentioned above. The lower sheet resistances of AZO-based composite films were verified experimentally by comparing with the ZnO/AgNW/ZnO composite electrode. (Supporting Information, Figure S2) The AZO layer conformally overcoats the AgNWs by occupying the empty spaces
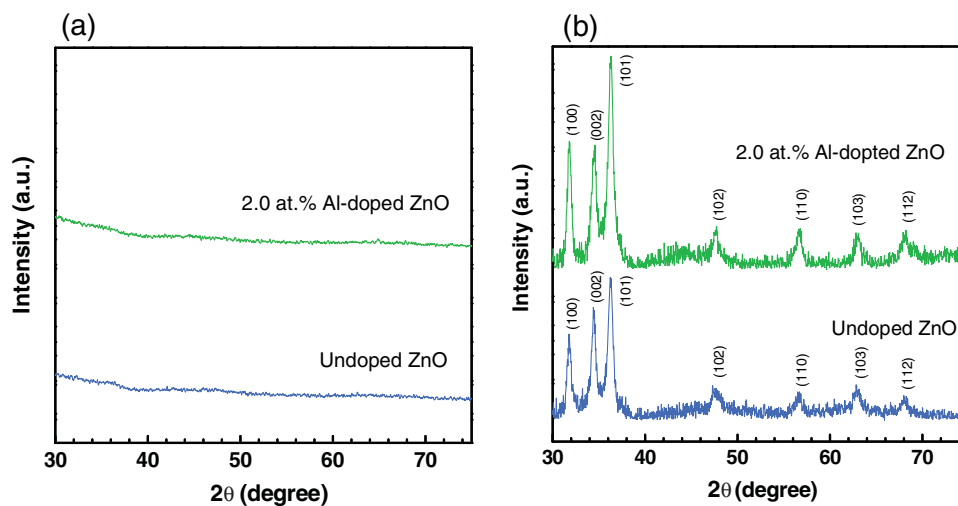

Figure 2. X-ray diffraction patterns of a) conventional sol–gel-derived, b) combustion sol–gel-derived ZnO and AZO thin films annealed at 200 °C. The peak positions are indexed to hexagonal ZnO (JCPDS #36–1451).
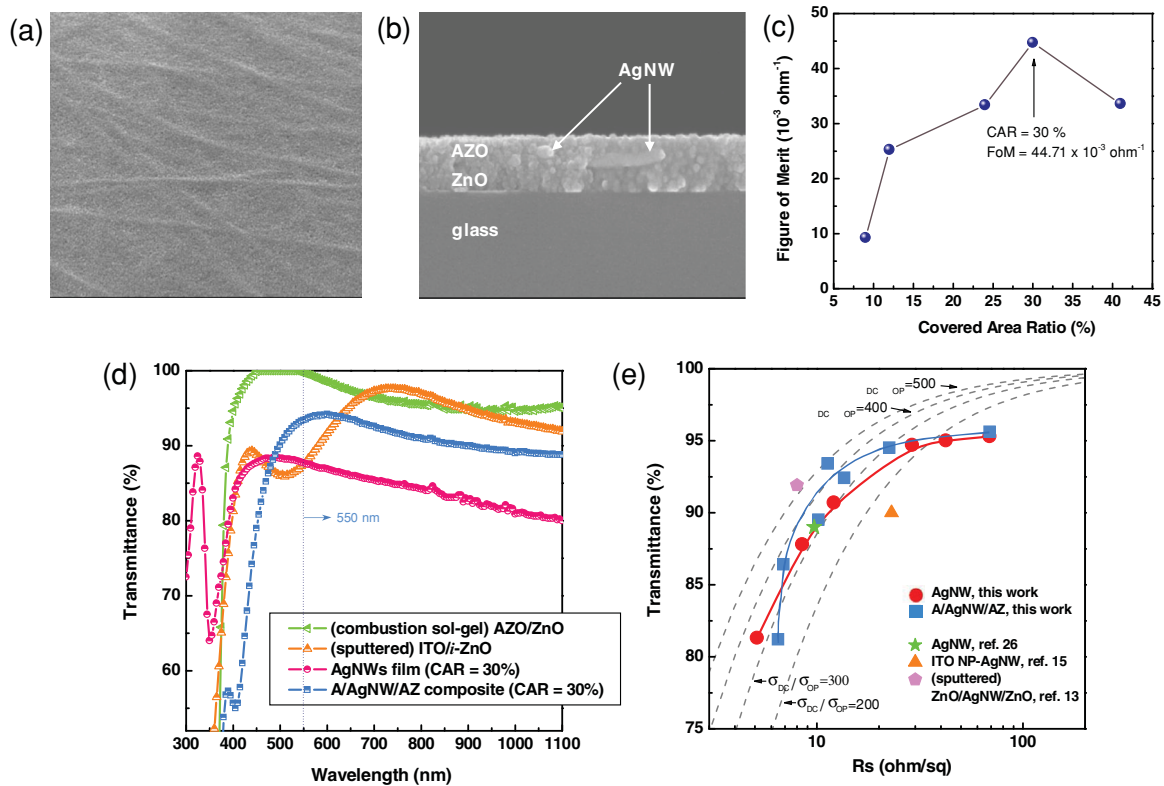
Figure 3. Scanning electron micrograph of a) a planar view and b) a cross section of the A/AgNW/AZ composite film. c) Figure of merit (FoM) values for the A/AgNW/AZ electrodes as a function of the CAR in the range of 9–41%. d) Transmittance spectra of the sputtered ITO/*i*-ZnO, an A/AgNW/AZ film, an AZO/ZnO film, and a bare AgNW film. e) Transmittance (550 nm) plotted as a function of the sheet resistance for an AgNW film, ZnO/AgNW/ZnO, and an A/AgNW/AZ composite electrode.

between the AgNWs. Although the AgNWs were chemically exposed to the spin-cast AZO precursor solution and underwent a subsequent annealing step at 200 °C, they maintained their original morphologies (28–35 nm diameters, >20 μm lengths). The surface of the AgNW film becomes smoother, depending on the thickness of the upper AZO layer. A rough, bare AgNW film can cause hazing due to diffuse reflection, while the specular reflectance of a perfectly flat surface can reduce the transmittance of the composite films; thus, we intentionally produced a composite electrode with a slightly rough surface (mean roughness ≈ 4.2 nm) by applying an AZO top layer with a thickness of ≈50 nm to obtain the desired reflectance. At 550 nm, the reflectance of the A/AgNW/AZ/glass was 6.7%, while that of the sputtered ITO/*i*-ZnO/glass was 20.3% (Supporting Information, Figure S3). A cross-sectional scanning electron microscopy (SEM) image shows the dense structure of the composite electrode in which the AgNWs are tightly embedded between the lower and upper metal-oxide layers (Figure 3b). This structure indicates that the electrical transport can be made more efficient and the scattering reduction in the composite electrodes compared with previously reported TCO nanoparticle-based particulate structures. The sheet resistance (R_S) and transmittance (*T*) of the A/AgNW/AZ composite electrodes are closely related to the AgNW density. We varied the AgNW density by adjusting the rotation speeds during the spin coating step for the AgNW

dispersion. The covered area ratio (CAR) was used to describe the different AgNW densities in the A/AgNW/AZ composite films. The CAR, a simple method for characterizing the optical and electrical properties of AgNW films, represents the fraction of the area occupied by the AgNWs. We quantified the CAR via image analysis using SEM images for the AgNW films spin-coated at different speeds. The detailed conversion process was described in our previous work.[13] Both R_S and *T* decrease with increasing AgNW density. To determine the optimum CAR for the AgNW film in the A/AgNW/AZ composite electrodes, the R_S and *T* values at 550 nm were used to calculate the figure of merit (Φ_{TC}) as defined by the Haacke equation[24]

$$\Phi_{TC} = \frac{T^{10}}{R_S} \tag{1}$$

Figure 3c depicts the calculated Φ_{TC} as a function of the CAR. The Φ_{TC} values increased with increasing CAR up to 30%. The maximum Φ_{TC} value was 44.7×10^{-3} Ω^{-1} (*T*: 93.4%, R_S: 11.3 Ω sq^{-1}) when the CAR was 30%.

The optical properties of our A/AgNW/AZ composite electrode were compared with those of various other transparent electrodes such as sputtered ITO/*i*-ZnO, AZO/ZnO bilayers (without AgNW), and bare AgNW films (Figure 3d). The transmittance of the top window layer is important in determining the amount of light that reaches the absorber layer and, in turn,
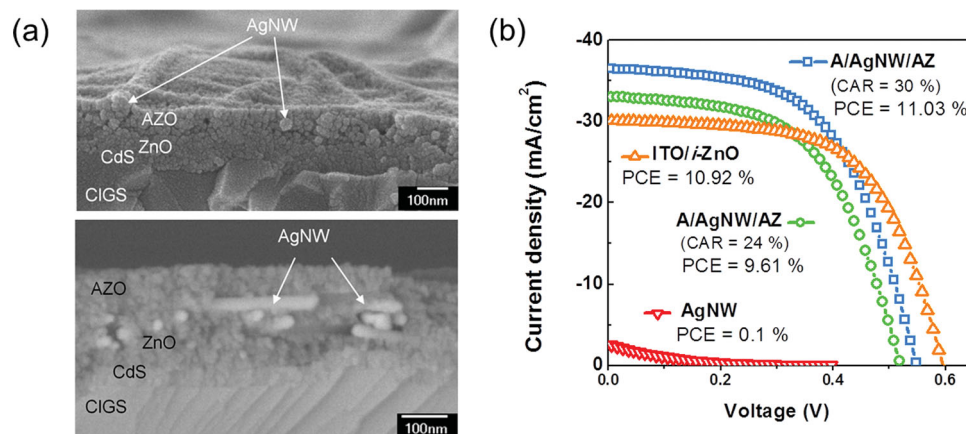
ADVANCED
FUNCTIONAL
MATERIALS
www.afm-journal.de

FULL PAPER

Materials Views
www.MaterialsViews.com

Figure 4. a) The upper SEM image presents a cross section of the $Cu(In_{1-x},Ga_x)S_2$ device with an A/AgNW/AZ composite electrode. The bottom provides a back-scattered electron (BSE) image demonstrating the composition contrast of the composite electrode on the device. b) Current density–voltage (J–V) characteristics for the thin-film solar cells based on the various top (window) electrodes.

the solar cell performance. The AZO/ZnO bilayer (without AgNW) exhibited optical transmittance values over 95% in the visible region. Our A/AgNW/AZ composite layer exhibited higher transmittance than the ITO/*i*-ZnO and the bare AgNW film in the visible range of 480–630 nm. At 550 nm, the *T* value of the A/AgNW/AZ composite was 93.4%, whereas the *T* values of ITO/*i*-ZnO and the bare AgNW film were 87.5% and 87.7%, respectively. For a clear comparison of the R_S and *T* characteristics, plots of *T* versus R_S at $\lambda = 550$ nm are presented in Figure 3e. The optimal previously reported results for AgNW transparent conductors with solution-processed ITO nanoparticle–AgNW composite electrodes, including our previous work, and sputtered ZnO/AgNW/ZnO composite electrodes are also indicated in Figure 3e. The relationship between *T* and R_S for a thin metallic film can be expressed as

$$T(\lambda) = \left(1 + \frac{188.5}{R_S}\frac{\sigma_{Op}(\lambda)}{\sigma_{DC}}\right)^{-2} \quad (2)$$

where $\sigma_{Op}(\lambda)$ is the optical conductivity (at 550 nm) and σ_{DC} is the DC conductivity of the film.[4,25] The σ_{Op}/σ_{DC} ratio is used as another figure of merit for an intuitive comparison of the R_S–*T* plots. A series of dotted grey lines represents the curves fitted according to Equation (2) when σ_{DC}/σ_{Op} corresponds to 500, 400, 300, and 200. A value of $\sigma_{DC}/\sigma_{Op} = 500$ is observed for the conventional ITO film and the high-performing nanostructured thin film.[4] Our solution-processed A/AgNW/AZ composite electrode is clearly superior to the state-of-the-art AgNW transparent electrode[26] and ITO nanoparticle–AgNW composite electrode.[15,16] Although the R_S values for A/AgNW/AZ are slightly higher than those of the bare AgNW film with the same CAR due to the presence of a relatively high-resistivity AZO layer, our composite electrode demonstrates a higher transparency at 550 nm than the bare AgNW film due to a reduced hazing effect. When compared with the ITO nanoparticle–AgNW composite, our sol–gel-derived A/AgNW/AZ composite exhibited less transmittance loss due to its reduced layer thickness (A/AgNW/AZ composite, ≈150 nm; ITO nanoparticle–AgNW composite, ≈400 nm); thus, the thin top electrode

is advantageous for both high transmittance and a reduced usage of materials. In addition, the electrical conductivity of the composite electrode can be calculated easily, whereas the calculation of electrical conductivity of a bare AgNWs film is difficult, since the thickness of Ag NWs film is hard to define due to its non-uniform thickness. The conductivity of A/AgNW/AZ (CAR = 30%) was calculated as 5.90×10^3 S cm^{-1}; it was about 4 times higher than the conductivity, 1.40×10^3 S cm^{-1}, of sputtered ITO film.

Our solution-processed A/AgNW/AZ composite electrode was applied as a transparent window layer for thin-film solar cells through successive spin coating onto CdS/CIGS/Mo/glass. A cross-sectional SEM image revealed that the top surface has an undulated surface finish following the topography of the AgNW network because the layer is not sufficiently thick to completely flatten the surface (**Figure 4**a). A back-scattered electron (BSE) SEM image confirmed that the composite electrode forms a conformal interface without voids over the CdS/CIGS layer (Figure 4a). The performance of a solar cell employing an A/AgNW/AZ composite electrode was evaluated in comparison with other devices containing transparent electrode layers including sputtered ITO/*i*-ZnO and bare AgNW films. The current density–voltage (J–V) characteristics for each device are provided in Figure 4b, and the photovoltaic device parameters are listed in **Table 1**. The standard reference solar cell, with a configuration of sputtered ITO/*i*-ZnO on CdS/CIGS/Mo/glass, exhibited a power conversion efficiency (PCE) of 10.91%, a V_{OC} of 0.59 V, a J_{SC} of 30.11 mA cm^{-2}, and an FF of 60.96%. The device with an A/AgNW/AZ (CAR = 30%) composite electrode exhibited comparable parameters with a PCE of 11.03%, a V_{OC} of 0.54 V, a J_{SC} of 36.43 mA cm^{-2}, and an FF of 56.21%. For the A/AgNW/AZ (CAR = 24%) composite electrode, a slightly reduced cell performance (PCE of 9.60%, V_{OC} of 0.52 V, J_{SC} of 33.01 mA cm^{-2}, and FF of 55.98%) was observed. This subtle degradation results from a lower figure of merit for the composite electrode with a CAR of 24%, indicating the critical impact of the optoelectronic properties of the transparent, conductive window layer on the device performance. The external quantum efficiency (EQE) spectra of devices using an

www.MaterialsViews.com

ADVANCED
FUNCTIONAL
MATERIALS
www.afm-journal.de

FULL PAPER

Table 1. Performance comparison of the thin-film solar cells fabricated using different transparent window layers: a sputtered ITO/*i*-ZnO layer, A/AgNW/AZ (CAR = 30%, 24%), and a bare AgNW film (CAR = 30%).

Window Layer	R_S [Ω sq^{-1}]	T [%, 550 nm]	J_{SC} [mA cm^{-2}]	V_{OC} [V]	FF [%]	PCE [%]
ITO/*i*-ZnO (sputtered)	35	87.5	30.11	0.59	60.96	10.91
A/AgNW/AZ (CAR = 30%)	11.3	93.4	36.43	0.54	56.21	11.03
A/AgNW/AZ (CAR = 24%)	13.6	92.4	33.01	0.52	55.98	9.60
AgNW (CAR = 30%)	8.5	87.7	2.75	0.48	8.47	0.11

ITO/i-ZnO and A/AgNW/AZ (CAR = 30%, CAR = 24%) composite electrodes also reflect the figure of merit of each transparent electrodes (Supporting Information, Figure S4).

In contrast, the cell based on a bare AgNW film performed poorly as characterized by the extremely low J_{SC} shown in Figure 4b, which can be attributed to the loose contact between the one-dimensional AgNWs and the underlying rough CdS/CIGS layer (Supporting Information, Figure S5). In addition, the bare AgNW network film contains many empty spaces between the nanowires, which limit the contact area with the underlying buffer/absorber layers. This prevents the efficient collection of free charge carriers by the AgNW network film when the diffusion length of the charge carrier is shorter than

the void between the AgNW networks, despite the film's low sheet resistance of ≈10 Ω sq^{-1}.[27,28] This lateral charge collection issue can be resolved by filling the voids with conductive metal oxides.[15,16,28] To evaluate the lateral conduction behavior, conductive atomic force microscopy (C-AFM) was performed for the transparent conductive electrodes composed of a bare AgNW film, an A/AgNW/AZ composite, and an AZO/ZnO bilayer as shown in **Figure 5**. An external bias (3.7 V) was applied between the AFM probe and the silver layer deposited adjacent to each electrode. The lateral current was measured with a current compliance of 100 nA. The diameter of the AgNWs, as revealed via SEM, was approximately 30 nm, which is in good agreement with the results obtained from AFM
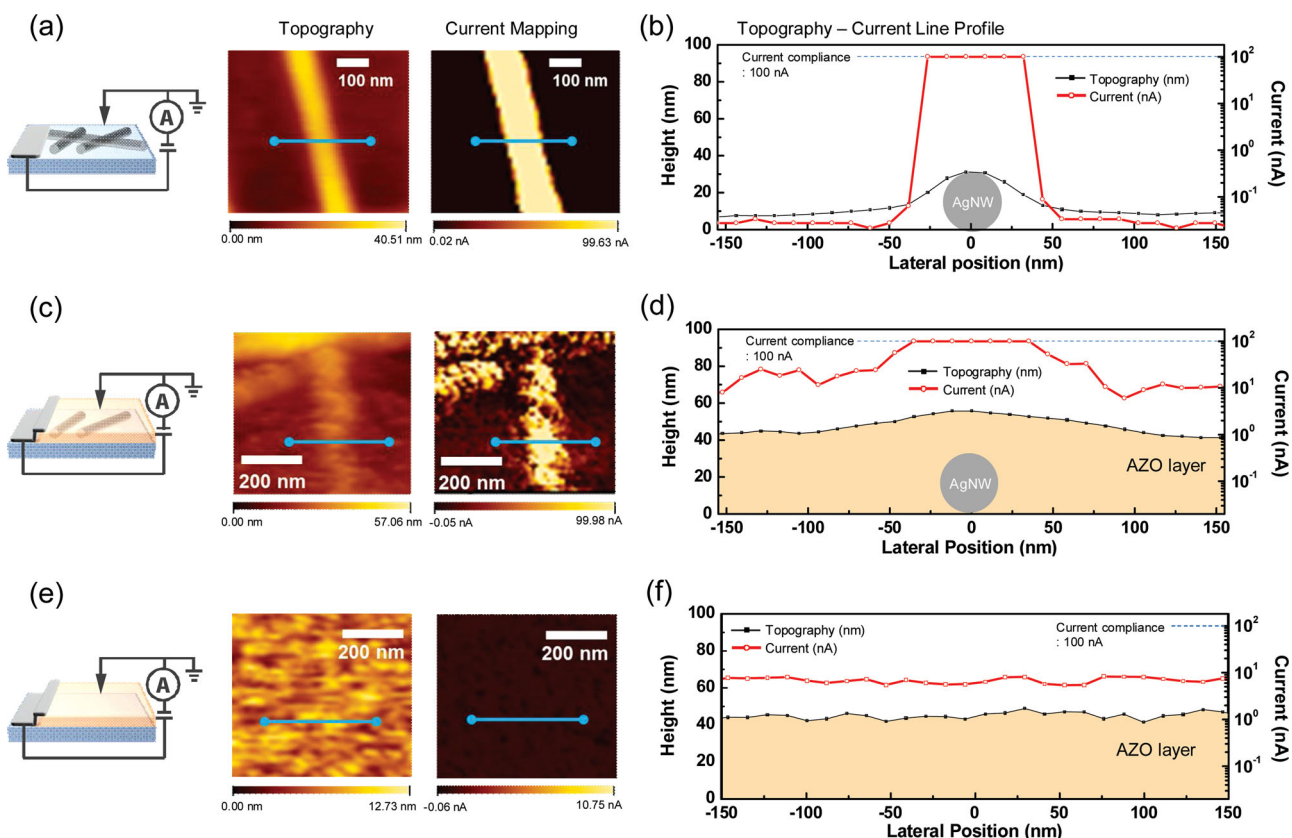

Figure 5. Topographic images and corresponding current maps for the different films on glass substrates; a) a bare AgNW film/glass, c) an A/AgNW/AZ composite/glass, e) AZO/ZnO/glass based on the conductive atomic force microscopy (C-AFM) measurements (the schematic diagrams on the left illustrate the sample setup). b,d,f) One-dimensional line profiles for the current and topography measured along the blue lines in the corresponding images.
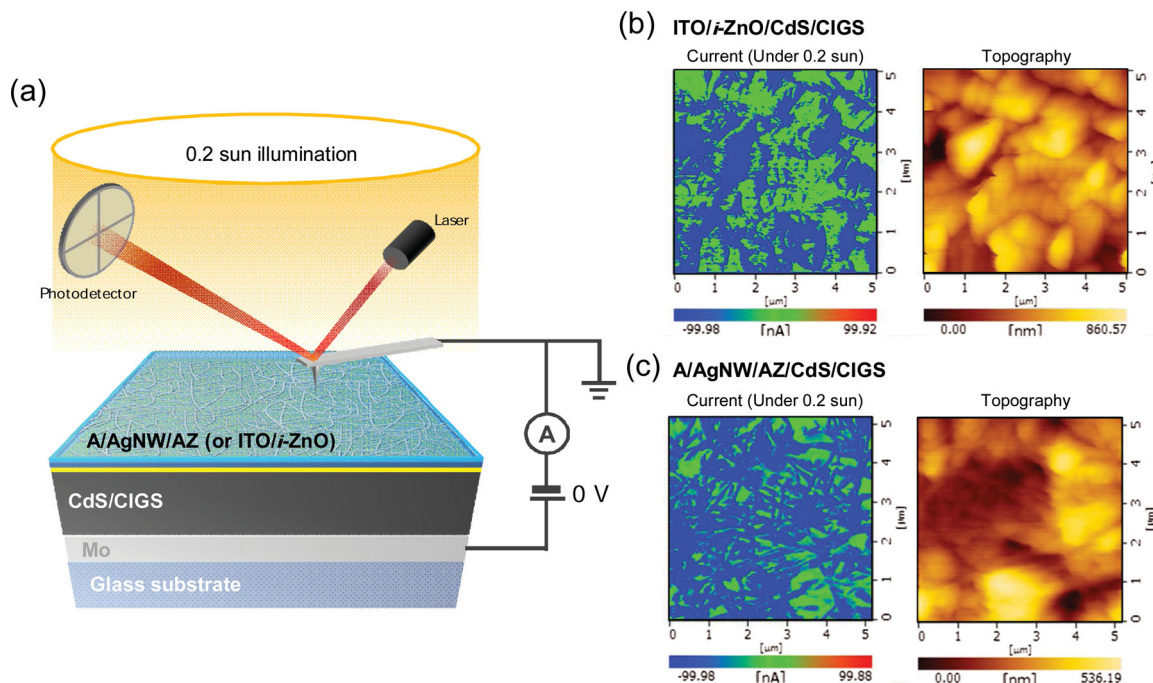
FULL PAPER

Figure 6. a) The system used for in situ current mapping of the thin-film solar cells under 0.2-sun illumination. b,c) In situ photocurrent mapping images acquired during the solar cell operation under 0.2-sun illumination and their corresponding topographic images.

topography analysis (Figure 5a,b), although a slight deviation occurred due to the tip-broadening caused by a tip curvature radius larger than the diameter of the AgNWs.[29,30] With the current mapping image (positive current), the width of the conductive region is wider (≈58 nm) than the diameter of the AgNWs due to the extended conduction under the external bias when the AFM probe approaches the AgNWs. The current apparently flows through the AgNW networks only for which the width of the maximum current region (100 nA, current compliance) is 58 nm, while no lateral transport of electrons occurs through the voids (Figure 5b). In contrast, for the A/AgNW/AZ composite electrode, the current flow was observed at locations containing no AgNWs. The A/AgNW/AZ composite film has a smoother surface than the bare AgNW film (Figure 5c), and lateral current conduction was observed for the composite electrode in a current mapping image (Figure 5d). Although the current primarily flowed through the AgNW networks, laterally conducting electrons were also detected in regions in which the metal oxides fill the inter-nanowire voids. In addition, the region exhibiting the maximum current extended further to ≈73 nm, indicating a broadening of the effective charge collection area. The current level decreased from ≈100 nA to ≈10 nA as the probe moved away from the center of the AgNW to ≈94 nm. The same measurements were performed for the AgNW-free AZO/ZnO bilayer (Figure 5e, f). Despite its uniform conduction, the average current level was significantly lower (≈9 nA) than that of the AgNW-embedded composite electrode film. The poor J–V performance of device employing the solution-processed AZO/ZnO film, shown in Figure S6 (Supporting Information), also demonstrates the fact that Ag NWs-free AZO/ZnO layers could not act as an effective electron collector. This result can be another distinct evidence

for the necessity of AgNWs insertion for solution-processed AZO matrix.

The lateral conduction behavior during solar cell operation in the absence of an external bias can provide valuable information regarding the transparent electrodes. To obtain local current measurements, we carried out a C-AFM analysis on the window electrode/CdS/CIGS/Mo/glass cells under light illumination. The AFM analyzes the signal from a coherent laser beam reflected from the back of an AFM cantilever. By detecting the beam deflection, the AFM can obtain nanoscale information on a sample surface. However, a 1-sun illumination from a xenon arc lamp, which is generally used to evaluate solar cell performance, is too intense and can disturb the laser signal transmitted to the photodetector. In a previous study mapping the photocurrents of solar cells, a ≈1-μm localized beam was used as an illuminator to prevent interference with the AFM laser signal.[31,32] However, localized beams generally consist of monochromatic light, which is unsuitable for comparing transparent electrodes with different wavelength-dependent transmittances. Instead, we used a xenon arc lamp with a spectrum that closely matched that of the sun and reduced the intensity to 0.2 sun, thus maintaining a sufficiently sensitive laser deflection signal. **Figure 6**a displays the C-AFM setup for an in situ photocurrent (negative current) map generated from the entire illuminated device. The in situ photocurrent mapping of the ITO/i-ZnO-based cell indicates that the measured photocurrents predominantly derive from the surface of the CIGS (Figure 6b). By matching the photocurrent map with a corresponding topographic image, the main conduction paths were found to include grain boundaries, grain surfaces, and surface defects such as the step edges of the CIGS film. By carefully examining the microstructures of all relevant surfaces,
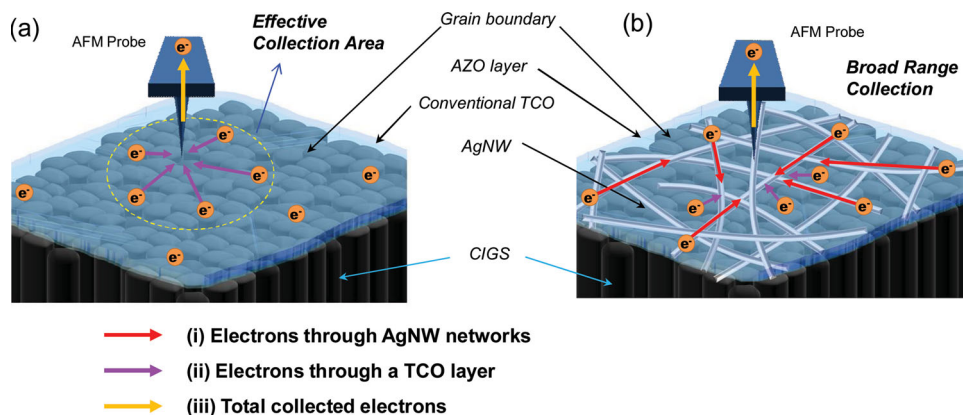
Scheme 1. Schematic diagrams of the electron collection path on the top contact of the thin-film solar cells. a) On the device with a metal-oxide/AgNW composite window layer, the electrons are transported and collected along at least two different pathways from the CIGS grains to the AFM probe. The AgNWs lying across grain boundaries provide a low-resistance pathway for the electrons. b) On the device with a metal-oxide window layer, the electrons are only transported through the metal-oxide layer from the CdS/CIGS surface to the AFM probe.

including the CIGS, CdS/CIGS, and ITO/*i*-ZnO/CdS/CIGS, one can conclude that the observed current pattern originates from the grain structure of the CIGS. A thin CdS layer with a thickness of ≈70 nm would not transform the micrometer-scale topology of the CIGS film, and the nanometer-scale grain structures of the crystallized ITO film were clearly distinct from those of the CIGS, as shown in Figure S7 (see Supporting Information). Although the nanometer-scale surface structures vary, the subsequent deposition of the thin layers (ITO ≈200 nm/*i*-ZnO ≈50 nm/CdS ≈70 nm) does not appear to significantly alter the microstructural features, which simply follow the surface geometry of the CIGS film. In contrast, the A/AgNW/AZ composite electrode-based device displays well-distributed photocurrents over the entire surface, as shown in Figure 6c. The photocurrent paths were primarily observed through the AgNW networks and were detected throughout a broader region depicted in blue in comparison with the reference device. This in situ photocurrent mapping is in good agreement with the overall cell performance characterized by the higher J_{SC} of the A/AgNW/AZ-based device compared with a reference cell. The schematics illustrate the mechanisms of photocurrent collection depending on the electrode type (**Scheme 1**). For the conventional TCO electrode-based cell, the electrons are transported only through the bulk TCO from an underlying CdS/CIGS film to the AFM probe (violet arrows in Scheme 1a). In contrast, in the A/AgNW/AZ-based device, at least two different pathways exist for transporting and collecting electrons from the underlying CdS/CIGS film to the AFM probe. One possible pathway is through the AgNW networks (red arrows in Scheme 1b). The AgNW networks located across the grain boundaries provide a faster and less resistive pathway than those through a bulk TCO film. As a second pathway, the electrons can be extracted through the AZO between the AgNWs, and then, they can be transported to the AgNW networks (violet arrows in Scheme 1b). In addition, the AgNW networks in the composite electrode can promote electron collection in regions farther from the metal probe (or the metal grid electrode) than the TCO top electrodes because the AgNWs can act as a broad-range collector due to their length, which is > 20 μm.

In addition to the higher J_{SC} observed for the composite electrode-based device, relatively low FF and V_{OC} values were observed, which may be associated with the optimization of the solution-processed *i*-ZnO layer. Although the role of an intrinsic ZnO layer remains controversial, it commonly acts as a shunt-preventing layer and an interfacial layer that adjusts the energy band alignment between the n-type buffer and the TCO electrode.[33,34] The cell fabrication process demonstrated in this study was optimized with sputtered *i*-ZnO, which is not a completely suitable solution-processed top contact given its thickness, resistivity, work function, etc. Thus, the solution-processed *i*-ZnO layer in the composite electrodes must be further optimized to improve the FF and V_{OC}. In addition, a scribing process should be considered to reduce the shunt leakage problem. We used a mechanical scribing method, which due to their ductile nature, may have resulted in drooping AgNWs at the cross section of the cell edge. This phenomenon can cause shunt leakage at the cell edges. Although some factors require further optimization as previously mentioned, the superior lateral conduction behavior of the composite electrode is promising for thin-film solar cell applications, especially for large size such as modules or panels by increasing the effective cell area. Scribed interconnection regions in monolithically integrated modules or shadow losses due to a metal grid in standard modules typically reduce the efficiency by 10–25%.[35] A transparent electrode with low sheet resistance and/or high lateral conductivity can reduce the dead space that results from scribing or the shadow of a front metal grid. We expect that more sparsely positioned front metal grids or scribe areas can be achieved by applying this AgNW-based composite electrode because metallic AgNW networks can provide fast and low-resistance lateral conduction paths by acting as small-scale metal grids. From an economic point of view, our composite electrode can significantly reduce the material cost. Indeed, the cost of Ag is not quite lower than the cost of indium (≈$23/oz for Ag and ≈$25/oz for In). Considering the amounts of indium and Ag utilized in each film with comparable T/R_S values, however, the cost-effectiveness of indium-free A/AgNW/AZ composite becomes obvious. The cost of Ag used in the

FULL PAPER

composite film (CAR = 30%, AgNW diameter = 30 nm) is 12 times less than the cost of indium in the commercial ITO film with 200 nm thickness. Moreover, this cost analysis was performed without taking into account on the manufacturing cost; therefore the overall cost of our solution-processed composite electrode can be much lower compared to vacuum-deposited conventional ITO film.

3. Conclusions

We prepared fully solution-processed, indium-free A/AgNW/AZ transparent composite electrodes, which were successfully implemented as the top transparent electrode in CIGS thin-film solar cells. With a unique combination of combustion sol–gel approach and conceptual approach of AgNW-ZnO composite structure, we could achieve the superior optical/electrical properties at a low temperature of 200 °C: high transmittance (93.4% at 550 nm) and low sheet resistance (11.3 Ω sq^{-1}), which are superior to those of state-of-the-art AgNW transparent electrodes and ITO nanoparticle–AgNW composite electrodes. The A/AgNW/AZ composite-based cell (PCE = 11.03%) slightly outperformed the sputtered ITO/i-ZnO-based device (PCE = 10.91%) as characterized by its superior J_{SC} value. We demonstrated that in situ C-AFM analyses under illumination can provide valuable information regarding the roles of different transparent electrodes applied to thin-film solar cells. The upper AZO layer enhanced the lateral conduction by filling the voids between the AgNWs and by tightening the electrical contact between the AgNWs and the underlying i-ZnO/CdS/CIGS layer. Furthermore, the A/AgNW/AZ composite effectively acted as a broad range collector of the photocurrents generated from the CdS/CIGS surfaces far from the AgNWs because a network structure of high-aspect-ratio AgNWs can provide a low-resistance, long-range pathway. Our indium-free A/AgNW/AZ composite may contribute to a cost-effective, sustainable high-performance thin-film solar cell by replacing the indium-containing or vacuum-deposited metal-oxide electrode layers. This composite electrode is expected to enhance the efficiency of large modules or panels by reducing the dead space caused by metal grids or scribed contacts because the AgNW networks can act as a nanoscale-metal grid over the cell surface.

4. Experimental Section

Preparation of the ZnO and AZO Sol–Gel Precursor Solution: Combustion method: Zinc nitrate hexahydrate (Zn(NO$_3$)$_2$·6H$_2$O, 99%, Alfa Aesar, Ward Hill, MA, USA) and zinc acetylacetonate (Zn(C$_2$O$_5$H$_5$)$_2$, 99.995%, Sigma Aldrich) were dissolved in 2-methoxyethanol (anhydrous, 99.8%, Sigma Aldrich) at a molar ratio of 1:1. The total concentration of the metal precursors was 0.15 M. Conventional method: The sol–gel solution used for ZnO was prepared by dissolving zinc acetate dihydrate (Zn(CH$_3$COO)$_2$·2H$_2$O, 99.999%, Sigma Aldrich) in 2-methoxyethanol (anhydrous, 99.8%, Sigma Aldrich). The total concentration of the metal precursors was 0.3 M. Ethanolamine (≥99.0%, Sigma Aldrich, St. Louis, MO, USA) was used as a stabilizing agent to improve the solubility of the precursor salts, and formamide (≥99.5%, Sigma Aldrich) was used to enhance the coating properties. For the AZO precursor solution, aluminum nitrate nonahydrate (Al(NO$_3$)·9H$_2$O, 99.997%, Sigma Aldrich) was further dissolved in the ZnO precursor solution to obtain Al/(Zn+Al) = 2 at% for both the combustion and

conventional methods. The precursor solutions were aged for 18 h prior to spin coating.

Composite Electrode Fabrication: The AZO/ZnO bilayer was prepared by successive spin coating. The ZnO bottom layer was deposited via spin coating at 2000 rpm for 30 s, followed by drying at 150 °C for 60 s. After 6 cycles of ZnO coating, the AZO layer was spin coated 8 times on the ZnO film at 2000 rpm for 30 s and dried under the same conditions. The AZO/ZnO film was annealed at 200 °C for 25 min. To prepare the AZO/AgNW/AZO/ZnO composite electrode, after 6 cycles of ZnO coating, the one layer of AZO was coated onto the ZnO layer. Then, the AZO/ZnO bilayer was annealed at 200 °C for 10 min. A UVO treatment was performed to remove any organic contaminants from the spin-cast AZO/ZnO prior to the AgNW film deposition. The AgNW density was controlled by the rotation speed used for the AgNW dispersion (AgNW-25, Seashell Technology, CA, USA). The AgNW films were dried at 150 °C for 60 s. A UVO treatment was also performed on the AgNW/AZO/ZnO film to remove any organic binders and additives from the AgNW film. The AZO top layer was then spin coated 7 times onto the AgNW/AZO/ZnO under the same spin-coating conditions. Finally, the composite films were annealed at 200 °C for 15 min. The schematic of the cross sectional image and the thickness information of the composite electrode comparing with sputtered ITO/i-ZnO film are in Figure S8 (see Supporting Information).

Optical, Structural, and Electrical Characterization: The optical transmittances of the transparent composite electrodes were measured at room temperature using a UV-vis spectrophotometer (V-530, Jasco, Oklahoma City, OK, USA). A bare glass substrate was used to obtain a baseline measurement. Spectral reflectance curves of the A/AgNW/AZ/glass and ITO/i-ZnO/glass were measured using a quantum efficiency measurement system (QEX10, PV Measurements, Inc., Boulder, CO, USA) equipped with an integrating sphere in the wavelength range of 300 to 1200 nm. The surface and cross section of the composite electrodes were analyzed via scanning electron microscopy (SEM, JSM-6010LV, JEOL Ltd., Tokyo, Japan) and atomic force microscopy (AFM, SPA 400, Seiko Instruments, Inc., Chiba, Japan). The surface roughness of the A/AgNW/AZ composite on a glass substrate was determined by AFM topography measurements. The sheet resistances of the A/AgNW/AZ samples were measured by a 4-point probe system (RS8, BEGA Technologies, Seoul, Korea) as a function of the AgNW densities expressed by the covered area ratio (CAR). The resistance reported herein is the average of a minimum of five measurements. The film crystallinity was determined using a multipurpose attachment X-ray diffractometer (Rigaku D/MAX-2500, TX, USA).

Thin-Film Solar Cell Fabrication: We used the same CIGS absorbers produced by co-evaporation (LG Innotek) to fabricate a solar cell for examining the influence of different transparent top electrodes. A CdS buffer layer of ≈70 nm was deposited via chemical bath deposition. The A/AgNW/AZ composite electrode was fabricated on the CdS/CIGS/Mo/glass as previously described. For the reference window layer, a 50-nm-thick i-ZnO layer was deposited via RF sputtering at a constant radio frequency (RF) power of 50 W at room temperature with a gas flow ratio of Ar:O$_2$ = 50 cc:5 cc under a working pressure of 1 mTorr. After deposition of the i-ZnO layer, a 200-nm-thick ITO layer was prepared via RF magnetron sputtering (RF power of 100 W at 200 °C, Ar flow rate of 50 cc, and working pressure of 1 mTorr). A solar cell containing only the AgNW film as a transparent electrode was also fabricated by spin coating the AgNW dispersion onto the i-ZnO/CdS/CIGS/Mo/glass substrate. Finally, dot-shaped silver front contacts were created on the window electrodes (diameter = 1 mm) using silver paste.

Characterization of the Thin-Film Solar Cells: The photovoltaic performance in terms of the J–V characteristics of the devices was determined using a solar simulator (Sol3A Class AAA, Oriel Instruments, Stratford, CT, USA) and a Keithley 2400 source measurement unit (Keithley Instruments Inc., Cleveland, OH, USA) under 1.5 air mass (AM) and 1 sun (100 mW cm^{-2}) conditions. The 1-sun intensity level was calibrated using a standard Si reference cell certified by the Newport Corporation. The PCE values were calculated from the measured J_{SC}, V_{OC}, and FF values by applying PCE = FF × V_{OC} × J_{SC}/P_s in which P_s

www.MaterialsViews.com

ADVANCED
FUNCTIONAL
MATERIALS
www.afm-journal.de

FULL PAPER

is the input solar irradiance (mW cm^{-2}). The FF term is defined as FF $= J_m V_m / J_{SC} V_{OC}$ in which J_m and V_m are the maximum current and voltage, respectively.

Conductive Atomic Force Microscopy (C-AFM): The C-AFM (AFM, SPA 400, Seiko Instruments, Inc., Chiba, Japan) analysis was performed using a rhodium-coated cantilever (SI-DF3-R, f = 27 kHz, C = 1.4 N/m) to obtain topographic images and current maps for the different top electrodes on both glass substrates and the CIGS solar cell devices. For lateral conduction analysis, a silver electrode was deposited onto the sides of the on-glass samples, and a bias of 3.7 V was applied between the side electrode and the AFM probe tip. Data were obtained at positions located ≈50 μm from the Ag side electrode to minimize measurement errors in the current level caused by the distance between the side electrode and the probe tip. Current profiles were extracted by scanning the line indicated in blue in Figure 5. For the in situ photocurrent mapping, the thin-film solar cells with an area of 5 μm × 5 μm were analyzed at a 0-V bias under a solar simulator light of 0.2 sun.

Supporting Information

Supporting Information is available from the Wiley Online Library or from the author.

Acknowledgements

[1] J. Krantz, T. Stubhan, M. Richter, S. Spallek, I. Litzov, G. J. Matt, E. Spiecker, C. J. Brabec, *Adv. Funct. Mater.* **2013**, *23*, 1711–1717.

[2] D. S. Hecht, L. Hu, G. Irvin, *Adv. Mater.* **2011**, *23*, 1482–1513.

[3] D. R. Cairns, R. P. Witte, D. K. Sparacin, S. M. Sachsman, D. C. Paine, G. P. Crawford, R. R. Newton, *Appl. Phys. Lett.* **2000**, *76*, 1425–1427.

[4] S. De, T. M. Higgins, P. E. Lyons, E. M. Doherty, P. N. Nirmalraj, W. J. Blau, J. J. Boland, J. N. Coleman, *ACS Nano* **2009**, *3*, 1767–1774.

[5] M. Kang, M. Kim, J. Kim, L. J. Guo, *Adv. Mater.* **2008**, *20*, 4408–4413.

[6] M. Vosgueritchian, D. J. Lipomi, Z. Bao, *Adv. Funct. Mater.* **2012**, *22*, 421–428.

[7] J. L. Blackburn, T. M. Barnes, M. C. Beard, Y. Kim, R. C. Tenent, T. J. McDonald, B. To, T. J. Coutts, M. J. Heben, *ACS Nano* **2008**, *2*, 1266–1274.

[8] A. A. Green, M. C. Hersam, *Nano Lett.* **2008**, *8*, 1417–1422.

[9] M. W. Rowell, M. A. Topinka, M. D. McGehee, H. Prall, G. Dennler, N. S. Sariciftci, L. Hu, G. Gruner, *Appl. Phys. Lett.* **2006**, *88*, 233506–233506–3.

[10] K. Kim, Y. Zhao, H. Jang, S. Lee, J. Kim, K. S. Kim, J. Ahn, P. Kim, J. Choi, B. Hong, *Nature* **2009**, *457*, 706–710.

[11] Y. Shi, K. Kim, A. Reina, M. Hofmann, L. Li, J. Kong, *ACS Nano* **2010**, *4*, 2689–2694.

[12] J. Y. Lee, S. T. Connor, Y. Cui, P. Peumans, *Nano Lett.* **2008**, *8*, 689–692.

[13] A. Kim, Y. Won, K. Woo, C. Kim, J. Moon, *ACS Nano* **2013**, *7*, 1081–1091.

[14] T. Stubhan, J. Krantz, N. Li, F. Guo, I. Litzov, M. Steidl, M. Richter, G. J. Matt, C. J. Brabec, *Sol. Energy Mater. Sol. Cells* **2012**, *107*, 248–251.

[15] C. Chung, T. Song, B. Bob, R. Zhu, Y. Yang, *Nano Res.* **2012**, *5*, 805–814.

[16] C. Chung, T. Song, B. Bob, R. Zhu, H. Duan, Y. Yang, *Adv. Mater.* **2012**, *24*, 5499–5504.

[17] J. Ajuria, I. Ugarte, W. Cambarau, I. Etxebarria, R. Tena-Zaera, R. Pacios, *Sol. Energy Mater. Sol. Cells* **2012**, *102*, 148–152.

[18] M. Kim, M. G. Kanatzidis, A. Facchetti, T. J. Marks, *Nat. Mater.* **2011**, *10*, 382–388.

[19] S. Schoemaker, A. Rosin, T. Gerdes, M. Willert-Porada, T. Lüthge, *Eur. J. Glass Sci. Technol. Part A* **2009**, *50*, 82–84.

[20] M. Ohyama, H. Kozuka, T. Yoko, *J. Am. Ceram. Soc.* **1998**, *81*, 1622–2632.

[21] K. Wu, C. Wang, D. Chen, *Nanotechnology* **2007**, *18*, 305604.

[22] S. Kijima, T. Nakada, *Appl. Phys. Express* **2008**, *1*, 075002.

[23] M.-G Kim, J. W. Hennek, H. S. Kim, M. G. Kanatzidis, A. Facchetti, T. J. Marks, *J. Am. Chem. Soc.* **2012**, *134*, 11583–11593.

[24] G. Haacke, *J. Appl. Phys.* **1976**, *47*, 4086–4089.

[25] S. De, P. J. King, P. E. Lyons, U. Khan, J. N. Coleman, *ACS Nano* **2010**, *4*, 7064–7072.

[26] D. Leem, A. Edwards, M. Faist, J. Nelson, D. D. C. Bradley, J. C. Mello, *Adv. Mater.*, **2011**, *23*, 4371–4375.

[27] L. Hu, H. S. Kim, J.-Y. Lee, P. Peumans, Y. Cui, *ACS Nano* **2010**, *4*, 2955–2963.

[28] F. S. F. Morgenstern, D. Kabra, S. Massip, T. J. K. Brenner, P. E. Lyons, J. N. Coleman, R. H. Friend, *Appl. Phys. Lett.* **2011**, *99*, 183307.

[29] D. L. Sedin, K. L Rowlen, *Appl. Surf. Sci.* **2001**, *182*, 40–48.

[30] K. Shiramine, S. Muto, T. Shibayama, N. Sakaguchi, H. Ichinose, T. Kozaki, S. Sato, Y. Nakata, N. Yokoyama, M. Taniwaki, *J. Appl. Phys.* **2007**, *101*, 033527.

[31] D. C. Coffey, O. G. Reid, D. B. Rodovsky, G. P. Bartholomew, D. S. Ginger, *Nano Lett.* **2007**, *7*, 738–744.

[32] L. S. C. Pingree, O. G. Reid, D. S. Ginger, *Adv. Mater.* **2009**, *21*, 19–28.

[33] U. Rau, M. Schmidt, *Thin Solid Films* **2001**, *387*, 141–146.

[34] H. Cai, D. Zhang, Y. Xue, K. Tao, *Sol. Energy Mater. Sol. Cells* **2009**, *93*, 1959–1962.

[35] M. W. Rowell, M. D. McGehee, *Energy Environ. Sci.* **2011**, *4*, 131–134.